Monthly Notices
of the
ROYAL ASTRONOMICAL SOCIETY

MNRAS **468,** 239–249 (2017)
Advance Access publication 2017 February 9

doi:10.1093/mnras/stx320

Four new massive pulsating white dwarfs including an ultramassive DAV

Brandon Curd,[1,2★] A. Gianninas,[1★] Keaton J. Bell,[3,4] Mukremin Kilic,[1★] A. D. Romero,[5] Carlos Allende Prieto,[6,7] D. E. Winget[3] and K. I. Winget[3]

[1]*Homer L. Dodge Department of Physics and Astronomy, University of Oklahoma, Norman, OK 73019, USA*
[2]*Harvard-Smithsonian Center for Astrophysics, 60 Garden St, Cambridge, MA 02138, USA*
[3]*Department of Astronomy, University of Texas at Austin, Austin, TX 78712, USA*
[4]*McDonald Observatory, Fort Davis, TX 79734, USA*
[5]*Departamento de Astronomia, Universidade Federal do Rio Grande do Sul, Av. Bento Goncalves 9500, Porto Alegre 91501-970, RS, Brazil*
[6]*Instituto de Astrofísica de Canarias, E-38205 La Laguna, Tenerife, Spain*
[7]*Departamento de Astrofísica, Universidad de La Laguna, E-38206 La Laguna, Tenerife, Spain*

Accepted 2017 February 3. Received 2017 February 1; in original form 2016 July 7

ABSTRACT

We report the discovery of four massive ($M > 0.8\,M_\odot$) ZZ Ceti white dwarfs, including an ultramassive $1.16\,M_\odot$ star. We obtained ground-based, time series photometry for 13 white dwarfs from the Sloan Digital Sky Survey Data Release 7 and Data Release 10 whose atmospheric parameters place them within the ZZ Ceti instability strip. We detect monoperiodic pulsations in three of our targets (J1015, J1554 and J2038) and identify three periods of pulsation in J0840 (173, 327 and 797 s). Fourier analysis of the remaining nine objects does not indicate variability above the $4\langle A\rangle$ detection threshold. Our preliminary asteroseismic analysis of J0840 yields a stellar mass $M = 1.14 \pm 0.01\,M_\odot$, hydrogen and helium envelope masses of $M_H = 5.8 \times 10^{-7}\,M_\odot$ and $M_{He} = 4.5 \times 10^{-4}\,M_\odot$ and an expected core crystallized mass ratio of 50–70 per cent. J1015, J1554 and J2038 have masses in the range 0.84–0.91 $M_\odot$ and are expected to have a CO core; however, the core of J0840 could consist of highly crystallized CO or ONeMg given its high mass. These newly discovered massive pulsators represent a significant increase in the number of known ZZ Ceti white dwarfs with mass $M > 0.85\,M_\odot$, and detailed asteroseismic modelling of J0840 will allow for significant tests of crystallization theory in CO and ONeMg core white dwarfs.

Key words: stars: oscillations – white dwarfs.

1 INTRODUCTION

White dwarfs (WDs) are the inert remnants of stars with a zero-age main sequence (ZAMS) mass of less than $\approx 8\,M_\odot$. With nuclear burning having ceased, WDs radiate away their energy and cool as a result. As hydrogen atmosphere (DA) WDs age and cool, they evolve through the ZZ Ceti instability strip wherein they become pulsationally unstable. The subsequent *g*-mode oscillations are excited by driving in the partial ionization zone of hydrogen in the atmosphere of the WD (Fontaine & Brassard 2008; Winget & Kepler 2008). A detailed pulsational analysis of these modes provides stringent constraints on the stellar mass and the thickness of the surface hydrogen layer (Bischoff-Kim et al. 2014; Giammichele et al. 2016).

The extreme pressure and density present in cool WDs induce crystallization as thermal energy is lost (Abriksov 1960; Kirshnitz 1960; Salpeter 1961) and this crystallization releases latent heat that significantly slows the WD cooling rate (Van Horn 1968). Segretain et al. (1994) show that central crystallization in a WD releases enough energy to lengthen the cooling time by several Gyr. Crystallization also affects the pulsations (Hansen & Van Horn 1979). However, only high-mass WDs have significantly crystallized cores while they are in the ZZ Ceti instability strip (Lamb & Van Horn 1975). Motivated by the discovery of pulsations in the massive WD star BPM 37093 (Kanaan et al. 1992), Winget et al. (1997) show that the mean period spacing of radial overtones grows as the crystallized mass ratio increases. In the first applications of crystallization theory, Montgomery & Winget (1999) and Metcalfe, Montgomery & Kanaan (2004) obtain best-fitting solutions to the pulsation spectrum of BPM 37093 that indicate it is of mass $M \lesssim 1.1\,M_\odot$ with a crystallized mass ratio of $\approx$90 per cent. In an independent analysis, Brassard & Fontaine (2005) conclude that the crystallized mass ratio lies between 32 and 82 per cent given the unknown chemical composition of the core.

Further evidence for core crystallization in cool WDs comes from Winget et al. (2009), whose analysis of the luminosity function and colour–magnitude diagram of the globular cluster NGC 6397 provides strong evidence for a first-order phase transition and the

★ E-mail: brandon.curd@cfa.harvard.edu (BC); alexg@nhn.ou.edu (AG); kilic@ou.edu (MK)

release of latent heat, which are central aspects of crystallization theory (Van Horn 1968). However, crystallization theory has yet to be thoroughly tested largely due to the lack of a large sample of high mass ($M > 0.8\,M_{\odot}$), variable DA WDs (or DAVs). The mass distribution of DAVs peaks at $\approx 0.6\,M_{\odot}$, with a tail towards higher masses (Lieberg, Bergeron & Holberg 2005; Kepler et al. 2007, 2015; Tremblay, Bergeron & Gianninas 2011; Kleinman et al. 2013). Given the historically small number of known WDs, the number of massive DAVs has only recently begun to grow significantly. This has led to difficulties to identify WDs on the high-mass end of the ZZ Ceti instability strip. In fact, the ultramassive regime ($M \geq 1.1\,M_{\odot}$) for DAVs, until now, was populated solely by BPM 37093 and GD 518 (Hermes et al. 2013).

The Sloan Digital Sky Survey (SDSS) has increased the number of spectroscopically confirmed WDs to about 30 000 (Harris et al. 2003; Kleinman et al. 2004, 2013; Esienstein et al. 2006; Kepler et al. 2015, 2016). Hence, the SDSS WD catalogues present an unprecedented opportunity to discover massive pulsating WDs and to eventually carry out rigorous tests of crystallization theory, which served as an impetus for this work. Mukadam et al. (2004), Kepler et al. (2005, 2012), Mullally et al. (2005), Castanheira et al. (2006, 2013) and Castanheira & Kepler (2009) have used the SDSS data to search for DAVs, including massive ones. Currently, there are about 200 DAVs known. Castanheira et al. (2013) studied the ensemble properties of high-mass DAVs and found evidence for a bimodal period distribution with no dominant pulsation periods near ≈500 s, which may be evidence of a mode selection mechanism. Romero et al. (2013) analysed the pulsation profiles of 42 high-mass DAVs with $1.05 > M > 0.72\,M_{\odot}$ and found that a crystallized interior yields best-fitting solutions for 15 stars. They also conclude that the mass of the hydrogen envelope in these stars ranges from 10^{-4} to $10^{-10}\,M_{*}$. The recent discovery of the most massive ($M = 1.20 \pm 0.03\,M_{\odot}$) DAV, GD 518, by Hermes et al. (2013) marks the beginning of the population of the extremely high-mass end of the ZZ Ceti instability strip. Such objects are likely the remnants of stars with a ZAMS mass of $\gtrsim 7\,M_{\odot}$ and could contain ONe or ONeMg cores as a result of carbon burning. Further populating the high-mass end of the ZZ Ceti instability strip will allow the ensemble characteristics of WDs in this regime to be analysed for the first time.

In this paper, we present results from multiple observations conducted on DAVs selected from the SDSS (York et al. 2000; Gunn et al. 2006; Abazajian et al. 2009; Eisenstein et al. 2011; Dawson et al. 2013; Smee et al. 2013; Ahn et al. 2014) Data Release 7 (DR7; Kleinman et al. 2013) and Data Release 10 (DR10) with the aim of discovering high-mass ($M > 0.8\,M_{\odot}$) DAVs. We report the successful detection of pulsations in four of our targets, including the most massive DAV in it, J0840, which is the second most massive DAV discovered to-date. In Section 2, we discuss the sample selection applied in this study. In Sections 3 and 4, we discuss our observations and analysis. In Section 5, we discuss the characteristics of our sample and conclude.

2 SAMPLE SELECTION

Our sample of targets consists of SDSS DR7 and DR10 WDs whose best-fitting atmospheric parameters place them within the empirical ZZ Ceti instability strip.

We select all targets with $T_{\rm eff} = 10\,000$–$13\,000$ K and $\log g > 8.5$ from the SDSS DR7 white dwarf catalogue of Kleinman et al. (2013) as objects of interest. For each of the 389 objects obtained in this first cut, we fit the normalized Balmer lines up to Hϵ of the SDSS spectra using the procedures described in Gianninas, Bergeron & Ruiz (2011). We identify 12 targets within the DR7 sample whose $T_{\rm eff}$ and $\log g$ are within the empirical boundaries of the ZZ Ceti instability strip (Gianninas et al. 2011) given the estimated errors. Kilic et al. (2015) photometrically identify one of these targets, J1529+2928, as a massive WD with a dark spot. Hence, J1529+2928 is excluded from the following discussion.

We also obtained spectral fits to ≈6000 DR10 WD spectra (identified by one of the authors, CAP) to search for additional targets. Given the number of potential targets in the DR10 sample, we only select the brightest and most massive objects ($g < 18.5$ mag, $M > 1.05\,M_{\odot}$) for follow-up observations. We identify four targets matching these criterion and were able to observe two (J0727 and J0840).

Fig. 1 presents our best fits to the normalized Balmer line profiles using ML2/$\alpha = 0.8$ 1D model atmospheres for our 13 massive DAV candidates. Table 1 presents the best-fitting parameters for these targets, including the 3D atmospheric corrections from Tremblay et al. (2013) and the average signal-to-noise ratio (S/N) of the SDSS spectrum. We computed the mass of each target using DAV cooling models described in Fontaine, Brassard & Bergeron (2001). As discussed in Gianninas, Bergeron & Fontaine (2005), since SDSS spectra are obtained over a set exposure time the S/N is significantly lower for fainter stars. For objects with an S/N of ∼20 (which is representative of our sample) the errors in effective temperature and surface gravity are as high as 400 K and 0.1, respectively. For such low S/N spectra this results in some ambiguity in selecting stars within the instability strip, especially near the edges of the strip. Nevertheless, we are confident that the solutions presented in Table 1 are accurate, but not precise, resulting in uncertainties of up to 7 per cent in our mass estimates. We discuss this in more detail in Section 4.

3 OBSERVATIONS

We obtained follow-up time series photometric data on the Gemini-North 8-m telescope, the ARC 3.5-m telescope at Apache Point Observatory (APO) and the Otto Struve 2.1-m telescope at McDonald Observatory.

We acquired high-speed photometry of 10 objects using the ARC 3.5-m telescope with the Agile frame transfer CCD with the *BG40* filter. Exposure times ranged from 30 to 60 s depending on the conditions and target brightness with uninterrupted integration times ranging from 0.6 to 1.8 h. We used the slow read-out setting and binned the CCD by 2 × 2, which resulted in a plate scale of 0.258 arcsec pixel^{-1}.

We acquired high-speed photometry of seven objects using the 2.1-m Otto Struve telescope with the ProEM camera and the *BG40* filter. Exposure times ranged from 5 to 25 s depending on the conditions and target brightness with total integration times on the order of 3–4 h. We binned the CCD by 4 × 4, which resulted in a plate scale of 0.36 arcsec pixel^{-1}.

We observed five objects using the 8-m Gemini-North telescope with the Gemini Multi-Object Spectrograph (GMOS) as part of the queue program GN-2015A-Q-86. We obtained time series photometry for each of these WDs with 10 s exposures through an SDSS g filter. We binned the CCD by 4 × 4, which yielded a read-out time and telescope overhead of ≈15 s and a plate scale of 0.29 arcsec pixel^{-1}. Given the queue program, some of our targets were observed for less than 30 min, which is sufficient to confirm relatively high-amplitude pulsations, as in J1554. However, the total integration times were insufficient to detect lower amplitude (and

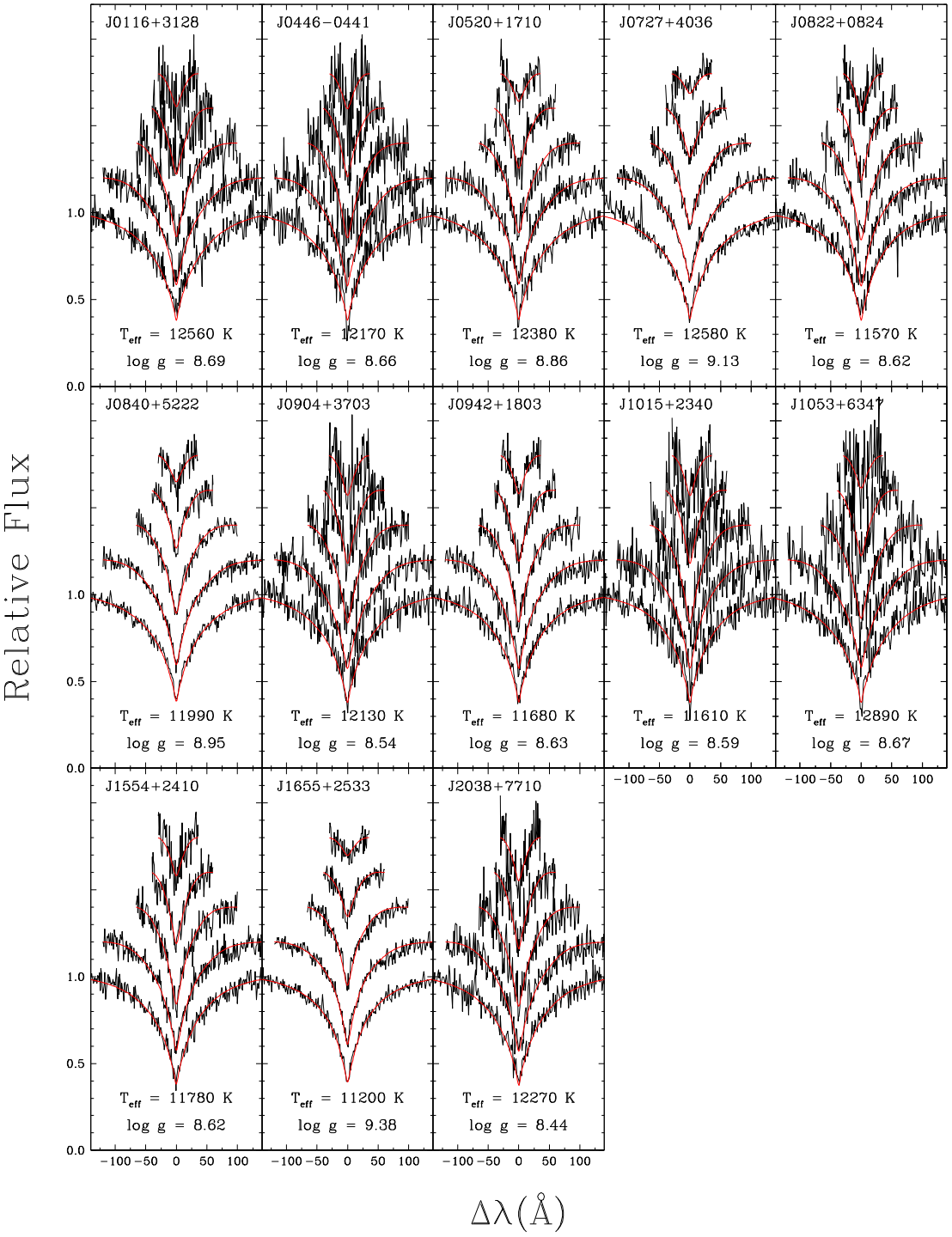

Figure 1. 1D model atmosphere fits to the normalized Balmer line profiles of our targets. The best-fitting parameters for each star are given in each panel.

possibly longer period) pulsations in some of the other Gemini targets. Table 2 presents the journal of observations.

For each object, we obtain bias and flat-field images and dark frames. We reduced the GMOS data using the standard Gemini GMOS routines under the Image Reduction and Analysis Facility (IRAF). We reduced the Agile and ProEM data using reduction routines in the IRAF IMRED package. We conduct aperture photometry on each object and nearby bright comparison stars in the images. We use IRAF DIGIPHOT for aperture photometry on the GMOS and Agile data, and the external IRAF package CCD_HSP (Kanaan, Kepler & Winget 2002) for aperture photometry on the ProEM data. To correct for transparency variations, we divide the sky-subtracted light curves by the weighted sum of the light curves of the nearest bright comparison stars in the field for each object. We fit a third-order polynomial to each calibrated light curve to remove the low-frequency signal ($P > 2000$ s) associated with a time-varying transparency. We note that our Fourier analysis only detects significant periods in the range of 150–1000 s and thus the removal of such low-frequency noise does not affect our conclusions. We compute the discrete Fourier transform (DFT) of the calibrated, pre-whitened

Table 1. Observational properties of our WD sample. The four pulsating WDs identified in this sample are denoted in bold text.

SDSS	g (mag)	S/N	$T_{\rm eff}$ (K)	$\log g$	Mass ($M_\odot$)	Period (s)	Amplitude (mma)[a]
J0116+3128	19.08	19	12 210 ± 370	8.64 ± 0.08	1.01 ± 0.05	–	<7.4
J0446−0441	19.56	17	11 830 ± 380	8.57 ± 0.09	0.97 ± 0.06	–	<21.6
J0520+1710	19.15	25	12 030 ± 310	8.78 ± 0.07	1.09 ± 0.04	–	<8.8
J0727+4036	18.10	38	12 350 ± 340	9.01 ± 0.07	1.20 ± 0.03	–	<9.4
J0822+0824	18.12	23	11 290 ± 230	8.47 ± 0.07	0.90 ± 0.05	–	<7.5
J0840+5222	18.24	36	12 160 ± 320	8.93 ± 0.07	1.16 ± 0.03	326.6 ± 1.3	7.1 ± 1.0
						172.7 ± 0.4	6.2 ± 1.0
						797.4 ± 8.0	6.3 ± 1.0
J0904+3703	19.09	18	11 800 ± 320	8.45 ± 0.08	0.89 ± 0.05	–	<6.7
J0942+1803	18.17	25	11 380 ± 210	8.49 ± 0.06	0.91 ± 0.04	–	<4.5
J1015+2340	18.67	14	11 320 ± 300	8.44 ± 0.10	0.88 ± 0.06	498.5 ± 4.9	15.7 ± 2.3
J1053+6347	18.65	16	12 590 ± 450	8.64 ± 0.09	1.01 ± 0.05	–	<7.3
J1554+2410	17.55	27	11 470 ± 230	8.49 ± 0.07	0.91 ± 0.04	673.6 ± 2.2	17.9 ± 1.1
J1655+2533	16.94	34	11 060 ± 170	9.20 ± 0.06	1.27 ± 0.02	–	<2.5
J2038+7710	19.05	20	11 940 ± 310	8.38 ± 0.08	0.84 ± 0.05	203.7 ± 0.1	16.3 ± 1.3

[a] 1 mma = 0.1 per cent relative amplitude.

Table 2. Journal of observations for the 13 ZZ Ceti candidates presented in this paper. Δt is the total integration time of the observations and $t_{\rm exp}$ is the exposure time of each individual frame.

SDSS	Instrument (telescope)	Filter	Date	$t_{\rm exp}$ (s)	Δt (h)	No. of points
J011647.94+312845.7	Agile (APO 3.5 m)	*BG40*	2015 Oct 12	45, 60	2.12	117
(J0116+3128)	ProEM (McDonald 3.5 m)	*BG40*	2014 Oct 30	5	3.81	2744
J044628.66−044125.5	ProEM (McDonald 2.1 m)	*BG40*	2015 Feb 02	30	3.88	466
(J0446−0441)	Agile (APO 3.5 m)	*BG40*	2015 Oct 12	45	2.44	127
J052016.37+171003.0	Agile (APO 3.5 m)	*BG40*	2014 Jan 28	30	1.46	112
(J0520+1710)	ProEM (McDonald 2.1 m)	*BG40*	2014 Oct 02	30	3.35	402
	ProEM (McDonald 2.1 m)	*BG40*	2014 Oct 03	30	3.53	423
	ProEM (McDonald 2.1 m)	*BG40*	2014 Oct 29	10	3.92	1411
	ProEM (McDonald 2.1 m)	*BG40*	2014 Oct 30	5	2.70	1942
	GMOS-N (Gemini 8.1 m)	*g*	2015 Feb 02	10	1.72	200
J072724.66+403622.0 (J0727+4036)	Agile (APO 3.5 m)	*BG40*	2016 Apr 05	40, 60	1.53	132
J082239.43+082436.7 (J0822+0824)	Agile (APO 3.5 m)	*BG40*	2014 Jan 28	30	1.01	121
J084021.23+522217.4	Agile (APO 3.5 m)	*BG40*	2016 Jan 15	45	0.87	49
(J0840+5222)	Agile (APO 3.5 m)	*BG40*	2016 Apr 04	40	1.92	161
	ProEM (McDonald 2.1 m)	*BG40*	2016 May 04	10	3.10	1117
	ProEM (McDonald 2.1 m)	*BG40*	2016 May 05	10	1.25	451
J090459.26+370344.4	ProEM (McDonald 2.1 m)	*BG40*	2016 Jan 13	10	3.06	1102
(J0904+3703)	Agile (APO 3.5 m)	*BG40*	2016 Jan 15	45	1.92	141
J094255.02+180328.6	GMOS-N (Gemini 8.1 m)	*g*	2015 Apr 09	10	0.93	132
(J0942+1803)	GMOS-N (Gemini 8.1 m)	*g*	2015 Apr 30	10	0.76	109
	GMOS-N (Gemini 8.1 m)	*g*	2015 May 18	10	0.50	72
J101540.14+234047.4 (J1015+2340)	GMOS-N (Gemini 8.1 m)	*g*	2015 Mar 03	10	1.15	163
J105331.46+634720.9 (J1053+6347)	Agile (APO 3.5 m)	*BG40*	2016 Jan 15	45	2.02	134
J155438.35+241032.6	GMOS-N (Gemini 8.1 m)	*g*	2015 Mar 16	10	0.18	27
(J1554+2410)	Agile (APO 3.5 m)	*BG40*	2015 Apr 09	45	1.96	123
	GMOS-N (Gemini 8.1 m)	*g*	2015 May 30	10	0.27	39
J165538.93+253346.0	GMOS-N (Gemini 8.1 m)	*g*	2015 Apr 17	10	0.09	32
(J1655+2533)	ProEM (McDonald 2.1 m)	*BG40*	2015 Aug 13	5	3.77	2711
J203857.52+771054.6	ProEM (McDonald 2.1 m)	*BG40*	2014 Aug 04	25	3.95	569
(J2038+7710)	Agile (APO 3.5 m)	*BG40*	2014 Aug 24	40	1.57	101
	ProEM (McDonald 2.1 m)	*BG40*	2014 Sep 02	20	4.29	773

light curves up to the Nyquist frequency using the software package PERIOD04 (Lenz & Breger 2005) and estimate the error associated with each period and amplitude using the Levenberg–Marquardt method as described in Bevington (1969). We consider periods of amplitude greater than $4\langle A\rangle$ (as opposed to the less conservative 3σ threshold) to be a positive detection of pulsations, where $\langle A\rangle$ is the average amplitude of the DFT up to the Nyquist frequency. Breger et al. (1993) suggest that using an S/N amplitude ratio of $\approx$4 appropriately differentiates real and false detections in pulsation analysis.

4 ANALYSIS

Here we describe the properties of each discovered DAV including the period(s) and amplitude(s) detected in our Fourier analysis. We then characterize the targets in our sample for which we did not detect pulsations and discuss possible reasons for the large number of non-DAVs in our sample. Lastly, we describe the results from our asteroseismic analysis of J0840.

4.1 Newly discovered DAVs

4.1.1 J0840

J0840 is the most massive DAV in our sample with $M = 1.16 \pm 0.03\,\mathrm{M}_\odot$, $T_{\rm eff} = 12\,160 \pm 320$ K and $\log g = 8.93 \pm 0.07$. Fig. 2 presents the APO and McDonald high-speed photometry observations of J0840, along with the DFT of the APO data from UT 2016 April 4. There are three significant frequencies, with the dominant period at $P = 326.6 \pm 1.3$ s with $A = 7.1 \pm 1.0$ mma amplitude, and two other frequencies at $P = 797.4 \pm 8.0$ and 172.7 ± 0.4 s with amplitudes $A = 6.3 \pm 1.0$ and 6.2 ± 1.0 mma, respectively. Table 3 presents the periods and amplitudes of pulsation and the detection limits for each night of observations.

We confirm all three periods with the McDonald 2.1-m telescope data from UT 2016 May 4 and 5, and also confirm the two shorter periods (174.6 ± 1.1 and 340.4 ± 4.3 s) with data from UT 2016 January 28. Given the different S/N of the light curves from each night, some of these modes fall below the $4\langle A\rangle$ limit, but they are persistent at both the APO and McDonald data, and therefore must be real. The computed amplitudes for the respective observations are consistent within the errors and thus these results do not indicate a modulation in the amplitude of these modes of pulsation. Our best data (UT 2016 April 4 and May 4) suggest that the two shorter periods ($P_1 \approx 330$ s and $P_2 \approx 170$ s) may be overtones as the frequencies are integer multiples of one another within the estimated errors.

4.1.2 J1015

J1015 is a DAV of mass $M = 0.88 \pm 0.06\,\mathrm{M}_\odot$ with $T_{\rm eff} = 11\,320 \pm 300$ K and $\log g = 8.44 \pm 0.10$. Fig. 3 shows the Gemini light curve of J1015 along with its DFT. J1015 displays significant pulsations with period $P = 498.5 \pm 4.9$ s and amplitude $A = 15.7 \pm 2.3$ mma. Follow-up observations to verify the dominant pulsation period of J1015 are needed. We note that the confirmation of a period of $P = 498.5 \pm 4.9$ s may contradict the suggestion made by Castanheira et al. (2013) that the DAV period distribution is bimodal and bereft of periods near $\approx$500 s.

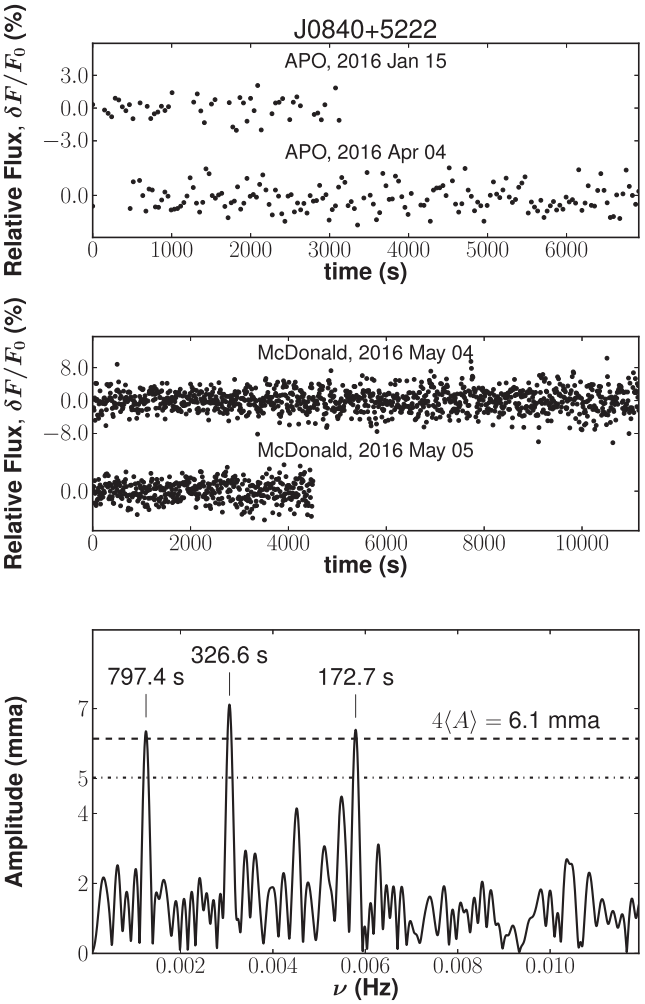

Figure 2. The light curves (top panels) and discrete Fourier transform (lower panel) from the longest integration time observations of SDSS J0840. In the lower panel, we indicate the $4\langle A\rangle$ (dashed line) and 3σ (dash–dotted line) detection limits.

Table 3. Periods, amplitudes and detection limits as determined for each night of observations for J0840.

Date	Period (s)	Amplitude (mma)	3σ (mma)	$4\langle A\rangle$ (mma)
2016 Jan 28	174.6 ± 1.1	6.7 ± 1.4	6.4	8.9
	340.4 ± 4.4	5.5 ± 1.4		
2016 Apr 04	172.7 ± 0.4	6.2 ± 1.0	5.0	6.1
	326.6 ± 1.3	7.1 ± 1.0		
	797.4 ± 8.0	6.3 ± 1.0		
2016 May 04	172.9 ± 1.0	8.1 ± 1.1	3.7	5.5
	328.8 ± 1.0	5.8 ± 1.1		
	817.6 ± 7.8	4.5 ± 1.1		
2016 May 05	172.6 ± 0.7	7.7 ± 1.5	5.3	7.8
	332.3 ± 3.4	6.4 ± 1.5		
	784.8 ± 17.7	6.0 ± 1.5		

4.1.3 J1554

J1554 is a DAV of mass $M = 0.91 \pm 0.04\,\mathrm{M}_\odot$ with $T_{\rm eff} = 11\,470 \pm 230$ K and $\log g = 8.49 \pm 0.07$. Fig. 4 shows

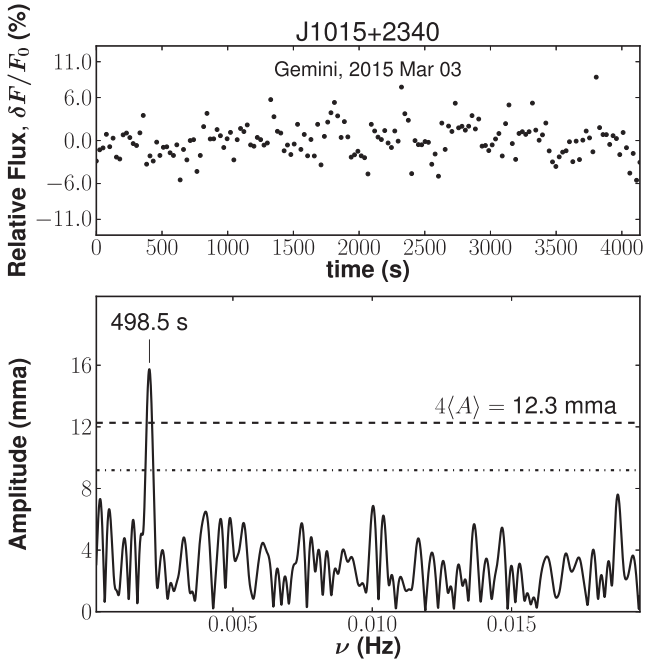

Figure 3. The light curve (top panel) and discrete Fourier transform (lower panel) of SDSS J1015. In the lower panel, we indicate the $4\langle A\rangle$ (dashed line) and 3σ (dash–dotted line) detection limits.

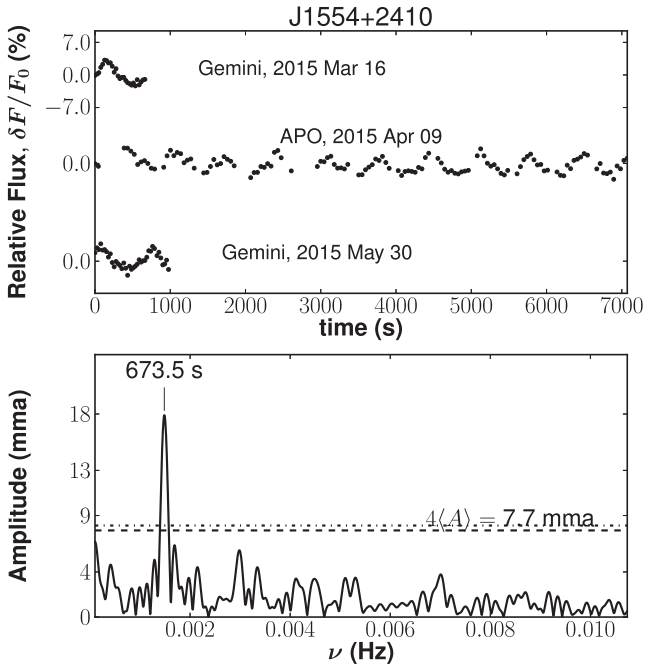

Figure 4. The light curves (top panel) and discrete Fourier transform (lower panel) from the longest integration time observations of SDSS J1554. In the lower panel, we indicate the $4\langle A\rangle$ (dashed line) and 3σ (dash–dotted line) detection limits.

the Gemini and APO data on J1554 along with the DFT of the longest light curve from APO observations on UT 2015 April 9. These data reveal a dominant pulsation mode at $P = 673.6 \pm 2.3$ s and amplitude $A = 17.9 \pm 1.1$ mma. On the other hand, the Gemini data show a significant peak at $P = 710.8 \pm 0.002$ s with an amplitude $A = 21.8 \pm 1.2$ mma. However, given the brevity of the combined Gemini-North observations (the total integration time is less than 2000 s), the change in amplitude is likely not real.

Table 4. Ensemble characteristics of synthetic light curves of J1554. Note that σ is the standard deviation of the 'noise function', $A_{\rm min}$ is the smallest computed amplitude, $A_{\rm max}$ is the largest computed amplitude and dA is the range of the set of solutions. Input parameters are $A_0 = 17.9$ mma, $f_0 = 1\,487.8$ μHz, $\sigma_1 = 8.8$ mma and $\sigma_2 = 7.0$ mma.

Data set	σ	$A_{\rm min}$ (mma)	$A_{\rm max}$ (mma)	dA (mma)
APO	$0.5\sigma_1$	17.5 ± 0.6	18.3 ± 0.5	0.8
	σ_2	16.7 ± 0.9	19.6 ± 1.0	2.8
	σ_1	17.1 ± 1.0	20.2 ± 1.1	3.1
	$2\sigma_2$	15.9 ± 1.7	21.5 ± 1.8	5.6
Gemini	$0.5\sigma_1$	16.7 ± 0.7	18.9 ± 0.8	2.2
	σ_2	16.5 ± 1.1	19.3 ± 1.2	2.8
	σ_1	15.5 ± 1.5	20.0 ± 1.5	4.5
	$2\sigma_2$	16.2 ± 2.3	25.0 ± 2.6	8.9

To explore the effect of light-curve gaps and noise on the resulting frequency power spectrum, we created synthetic light curves that emulate the observations of J1554 (Table 2, Fig. 4) using a function of the form

$$A(t) = A_0 \sin(2\pi f_0 t) + N(\mu, \sigma), \quad (1)$$

where A_0 is the amplitude of the pulsation in mma, f_0 is the frequency of the pulsation in Hz and $N(\mu, \sigma)$ (or the 'noise function') is a random number generator that samples a normal distribution with mean μ and standard deviation σ. Note that we assume the presence of only one pulsation period (based on the APO observations, $A_0 = 17.9$ mma, $f_0 = 1\,487.8$ μHz) and that the noise is Gaussian. We derive σ from each respective pre-whitened light curve with the contribution from the pulsations subtracted. Given the small number of data points in the Gemini observations, we run six initializations for values of $\sigma = 0.5\sigma_1, \sigma_2, \sigma_1$ and $2\sigma_2$, respectively (where σ_1 is the standard deviation from UT 2015 April 09 and σ_2 is the standard deviation from UT 2015 March 16 and May 30).

We present the ensemble characteristics of our synthetic light curves for six initializations with σ held constant in Table 4. This analysis demonstrates that random noise and gaps result in a range of amplitude solutions of up to 8.9 mma in the most extreme case of $\sigma = 2\sigma_2$. Even if we consider a modest noise contribution of $\sigma = \sigma_2$, the smallest amplitude computed from the APO data ($A_{\rm min} = 16.7 \pm 0.9$ mma) and the largest amplitude computed from the Gemini data ($A_{\rm max} = 19.3 \pm 1.2$ mma) are not consistent given the estimated errors. We conclude that gaps and random noise, especially for small data sets, can result in amplitude solutions for two respective data sets that are inconsistent within the estimated errors despite the input amplitude remaining constant and thus we do not consider our observations of J1554 to be indicative of amplitude modulations. There is no evidence of amplitude modulations in our other DAVs with multiple nights of data. Montgomery & O'Donoghue (1999) show that non-linear least-squares errors can significantly underestimate the true error and should be treated as a lower limit, which further suggests that the inconsistency of amplitude and period solutions for J1554 is not strong evidence of modulations.

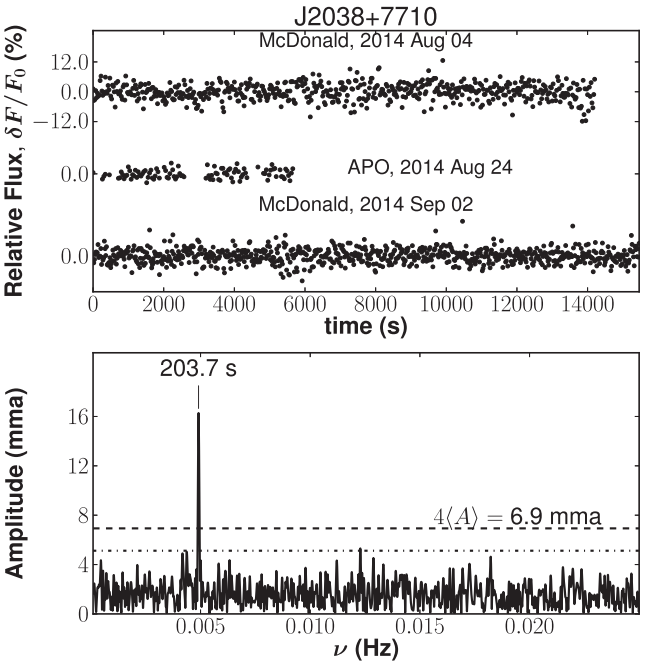

Figure 5. The light curves (top panels) and discrete Fourier transform (lower panel) from the longest integration time observations of SDSS J2038. In the lower panel, we indicate the $4\langle A\rangle$ (dashed line) and 3σ (dash–dotted line) detection limits.

4.1.4 J2038

J2038 is a DAV of mass $M = 0.84 \pm 0.05\,\mathrm{M}_\odot$ with $T_{\rm eff} = 11\,940 \pm 310$ K and $\log g = 8.38 \pm 0.08$. Fig. 5 shows the McDonald and APO light curves of J2038 along with the DFT of longest light curve from McDonald observations on UT 2014 September 2. J2038 displays significant pulsations with period $P = 203.7 \pm 0.1$ s and amplitude $A = 16.3 \pm 1.3$ mma. We also compute the DFT using data from McDonald, 2014 September 02 (APO, 2014 August 24) and detect a period of $P = 203.8 \pm 0.2$ (203.4 ± 0.2) s and amplitude of $A = 17.7 \pm 1.8$ (18.5 ± 1.1) mma. The computed amplitudes are consistent within the errors and thus these results do not indicate a variation in the amplitude of the dominant period of pulsation.

4.2 Non-DAVs

Figs 6 and 7 display light curves and DFTs of the longest integration time observations of the nine non-DAVs in our sample. Our $4\langle A\rangle$ detection limits for these objects range from 2.5 mma for J1655 to 21.6 mma for J0446. We note that all but one of the objects (J1655) for which pulsations were not detected have spectroscopically determined atmospheric parameters that indicate they should undergo pulsations (Fig. 8). We computed the photometric temperature from the SDSS photometry following the procedure outlined by Bergeron, Ruiz & Legget (1997) and assuming $\log g = 8.5$ for all 13 targets. We find good agreement between the photometric and spectroscopic solutions for all objects but J0520, J0727 and J0822 (see Fig. 9). The photometric solutions for J0520 and J0822, respectively, are significantly cooler than the spectroscopic models and would place them outside of the ZZ Ceti instability strip. However, the photometric temperature solution for J0727 (which is roughly 1000 K hotter) is still within the bounds of the ZZ Ceti instability strip given its high surface gravity.

The rest of the non-variable objects are close to the red edge of the instability strip. Given the relatively low S/N of the SDSS spectra, the best-fitting temperature solutions for these stars are within 1σ–2σ of the empirical red edge, hence we suspect that some of these stars might have already evolved outside of the instability strip. Another alternative is that our $4\langle A\rangle$ detection limits are not stringent enough to detect low-amplitude pulsations in these stars. For example, we detect a single low-amplitude period below the $4\langle A\rangle$ threshold but above the 3σ level for both J0727 and J1053. J0727 shows a dominant period at $P = 100.54 \pm 0.97$ s and amplitude $A = 6.66 \pm 1.76$ mma, whereas J1053 shows a dominant period at $P = 120.21 \pm 0.25$ s and amplitude $A = 6.79 \pm 1.37$ mma. These periods lie within the observed range of periods for DAVs, which is roughly 100–2000 s. J0520 and J0904 also showed a significant period above the 3σ threshold on one night (2014 October 29 and 2016 January 15, respectively); however, no subsequent detections were made in any of the other available light curves. A better sampling rate and longer integration time would significantly improve the S/N in the DFT and may reveal these periods to be indicative of real pulsations.

Given the relatively short time span of our observations of some of the non-DAVs and our detection limits, it is possible that several of these WDs may exhibit lower amplitude pulsations that would escape detection in our light curves. For example, several DAVs presented in Castanheira et al. (2013) and Romero et al. (2013) have dominant periods of pulsation with amplitudes lower than 5 mma. In addition, J0840, a newly discovered DAV in our sample, is another example of a ZZ Ceti WD with two low-amplitude pulsations with $A < 7$ mma that is below the computed detection threshold for both J0116 and J0446.

4.3 Preliminary asteroseismic analysis of J0840

We used the three detected pulsation periods from April 04 (see Table 3) to perform a preliminary asteorseismological analysis. The DAV models used in this work were generated using LPCODE evolutionary code (see Renedo et al. 2010 for details). We employed WD model sequences with stellar mass between 1.024 and 1.15 $\mathrm{M}_\odot$ and carbon–oxygen core. The sequences with stellar mass larger than 1.08 $\mathrm{M}_\odot$ were obtained by artificially scaling the stellar mass from the $\sim$1 $\mathrm{M}_\odot$ sequence at high effective temperatures, and the remaining ones are those presented in Romero et al. (2013).

Residual nuclear burning was not considered for the massive sequences, since they have relatively thin hydrogen envelopes. Crystallization processes and the additional energy sources are included following the Horowitz, Schnieder & Berry (2010) phase diagram. Note that the effective temperature where crystallization begins increases with stellar mass (Romero et al. 2013). For instance, crystallization starts at 14 500 K for 1.05 $\mathrm{M}_\odot$ and at 17 250 K for 1.14 $\mathrm{M}_\odot$. Finally, we computed non-radial g-mode pulsations using the adiabatic version of the LP-PUL pulsation code described in Córsico & Althaus (2006) (see Romero et al. 2012, 2013 for details), we consider $\ell = 1, 2$ modes.

Using the mass–radius relations from Romero et al. (2012) and Althaus et al. (2005) for the O/Ne core WDs, we determine a stellar mass of $1.13 \pm 0.05\,\mathrm{M}_\odot$. Note that the limiting mass for C/O core WDs is uncertain and it depends on the metallicity of the progenitor star. According to Doherty et al. (2015), for solar metallicity, the limiting mass is between 1.075 and 1.158 $\mathrm{M}_\odot$.

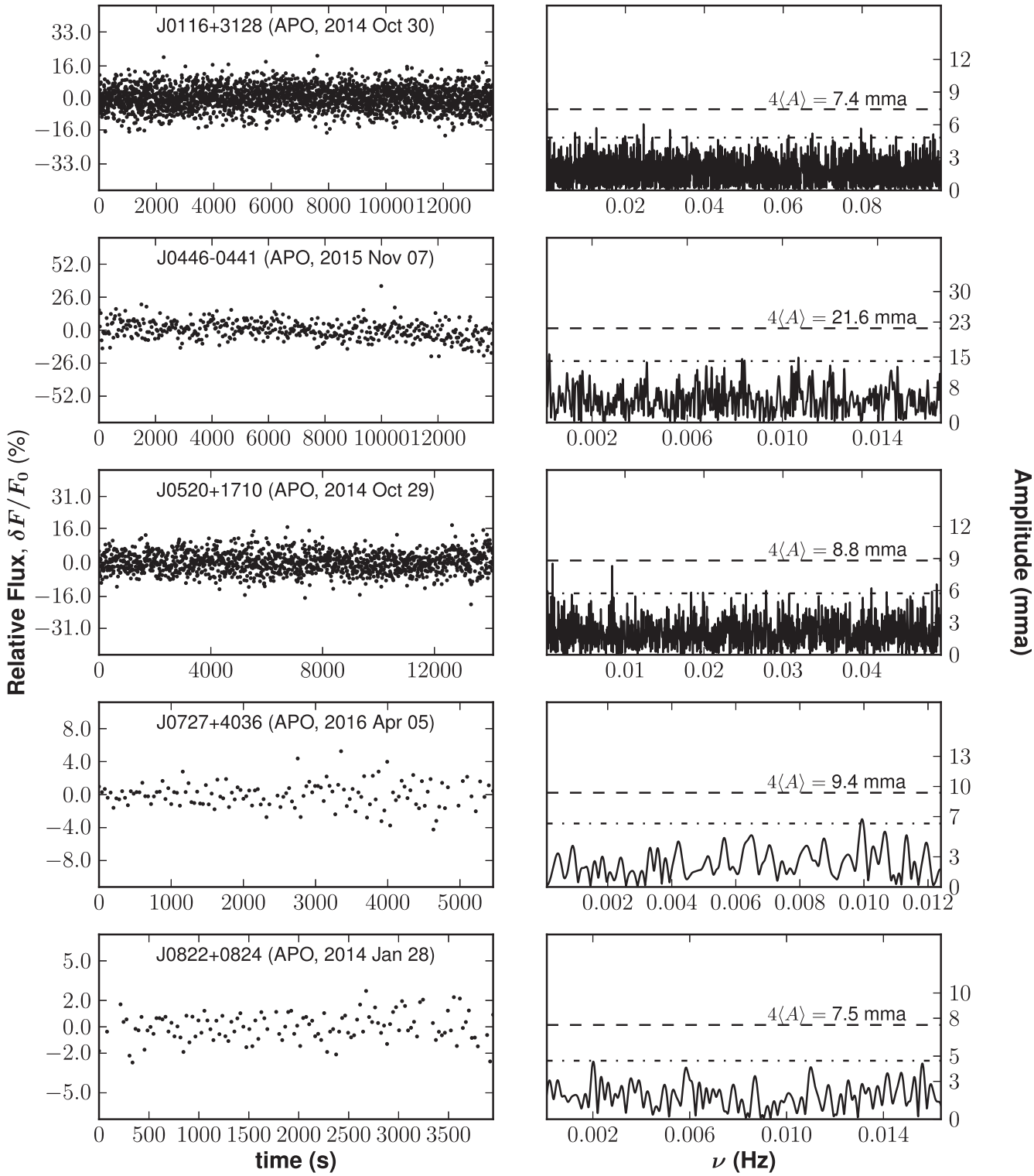

Figure 6. The light curve (left) and discrete Fourier transform (right) for the longest integration time observation for each respective WD in which we do not detect significant frequencies in the Fourier power spectrum. In the panels on the right, we indicate the $4\langle A\rangle$ (dashed line) and 3σ (dash–dotted line) detection limits.

To find the best-fitting model we minimize the quality function S:

$$S = \sqrt{\sum_{i=1}^{N} \frac{[\Pi_k^{\rm th} - \Pi_i^{\rm obs}]^2\, w_i}{\sum_{i=1}^{N} w_i}}, \qquad (2)$$

where N is the number of observed modes and w_i are the amplitudes. First we consider only monopole modes. We obtained a solution characterized by a stellar mass $M = 1.14\,{\rm M}_\odot$, $M_{\rm H} = 5.837 \times 10^{-7}\,{\rm M}_\odot$ and $M_{\rm He} = 4.455 \times 10^{-4}\,{\rm M}_\odot$, $T_{\rm eff} = 11\,850$ K, with theoretical periods 171.862 s ($l = 1$, $k = 3$),

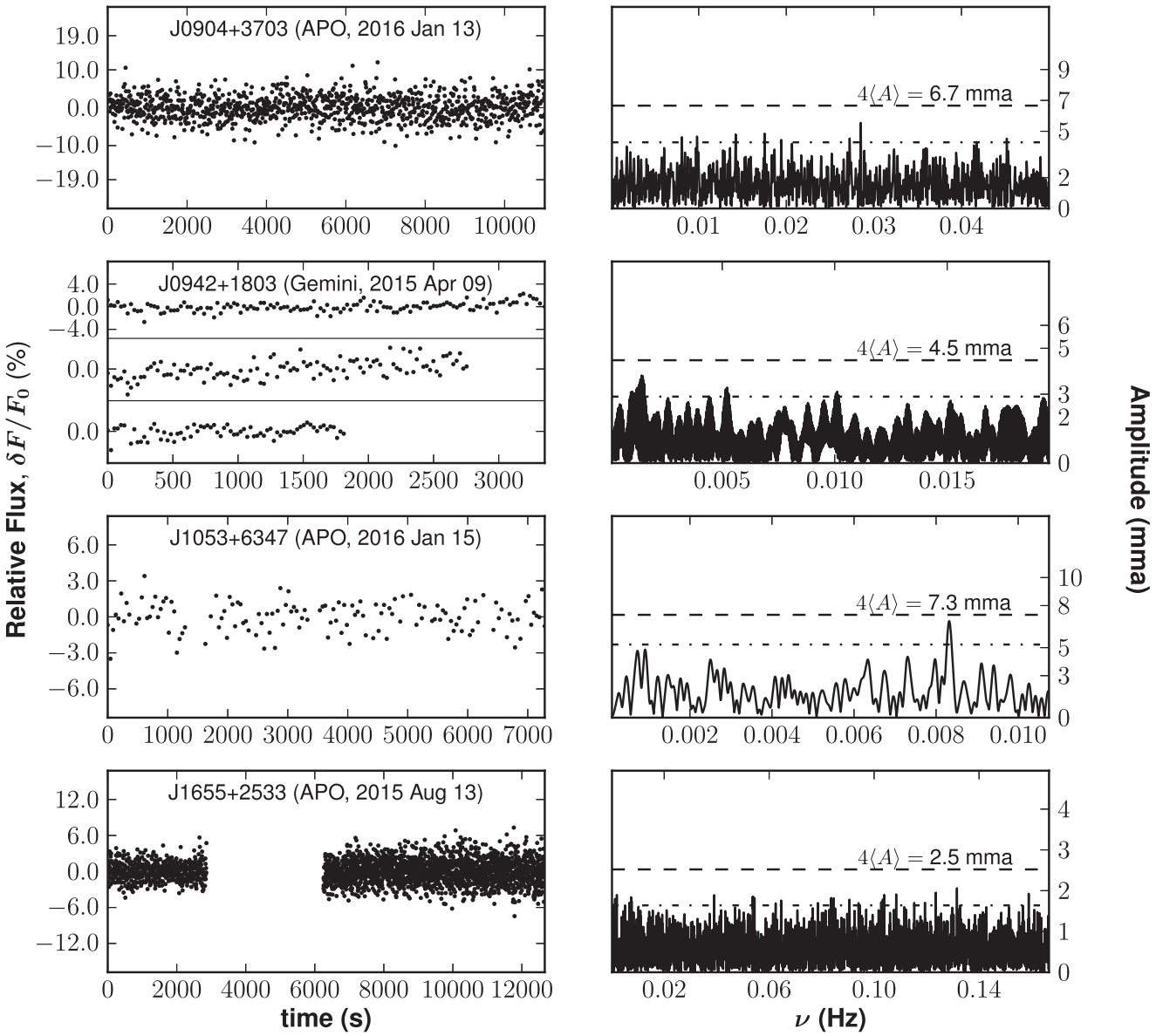

Figure 7. The light curve (left) and discrete Fourier transform (right) for the longest integration time observation for each respective WD in which we do not detect significant frequencies in the Fourier power spectrum. In the panels on the right, we indicate the $4\langle A\rangle$ (dashed line) and 3σ (dash–dotted line) detection limits.

320.013 s ($l = 1$, $k = 8$) and 798.773 s ($l = 1$, $k = 23$) and a value of $S = 4.06$ s. Note that this model shows a lower effective temperature than the spectroscopic value, but is still in agreement considering the uncertainties. We note from our fits that the dominant mode in determining the stellar mass is the mode ∼172 s, which is also the more stable mode throughout the different nights. In this fit, the mode 797.4 s is very well fitted but is also the mode with the larger uncertainty. Next, we include in our fit $\ell = 2$ modes, and in addition we consider the uncertainties in the periods. We obtain a representative model characterized by the same stellar mass and hydrogen mass as our previous fit, but with $T_{\rm eff} = 12\,200$ K and theoretical periods 170.557 s ($l = 1$, $k = 3$), 326.562 s ($l = 2$, $k = 15$) and 804.645 s ($l = 2$, $k = 40$).

It is important to note that with this set of periods, considering the uncertainties, the seismological effective temperature can vary from 11 850 to 12 350 K. On the other hand, the stellar mass is more constrained to $M_* = 1.14 \pm 0.01\,{\rm M}_\odot$, in well agreement with the spectroscopic value. Within this effective temperature range, it is expected that 50–70 per cent of the core mass is to be crystallized. In this scenario, the pulsation modes propagate in a small region of the star located mainly in the envelope of the star.

5 DISCUSSION AND CONCLUSIONS

We have confirmed pulsations in four DAVs with $M > 0.84\,{\rm M}_\odot$ including a $1.16 \pm 0.03\,{\rm M}_\odot$ WD (J0840). For the remaining nine targets in our sample we provided upper limits on their variability.

Our preliminary asteroseismic analysis of J0840 yields $M = 1.14 \pm 0.01\,{\rm M}_\odot$, $M_{\rm H} = 5.8 \times 10^{-7}\,{\rm M}_\odot$, $M_{\rm He} = 4.5 \times 10^{-4}\,{\rm M}_\odot$ and an expected core crystallized mass ratio of 50–70 per cent.

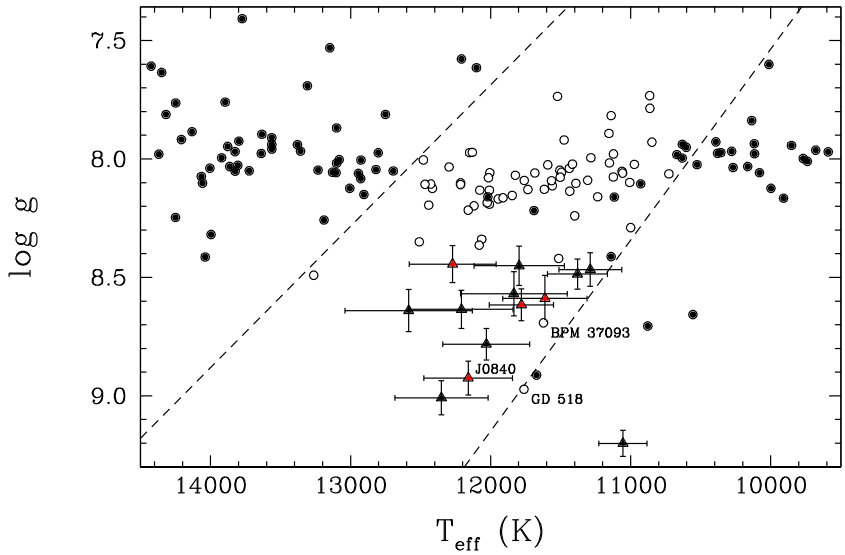

Figure 8. The 3D-corrected atmospheric parameters of the newly discovered ZZ Ceti WDs (red triangles) and non-DAVs (black triangles) along with those of known ZZ Ceti WDs (open circles) and non-variable WDs (filled circles). The atmospheric parameters of our newly discovered DAVs are consistent with the empirical bounds of the ZZ Ceti strip (dashed lines; Gianninas et al. 2011). Previously known DAVs/non-DAVs include BPM 37093 (Kanaan et al. 1992) and GD 518 (Hermes et al. 2013) and DAVs from Gianninas et al. (2011) and Green et al. (2011).

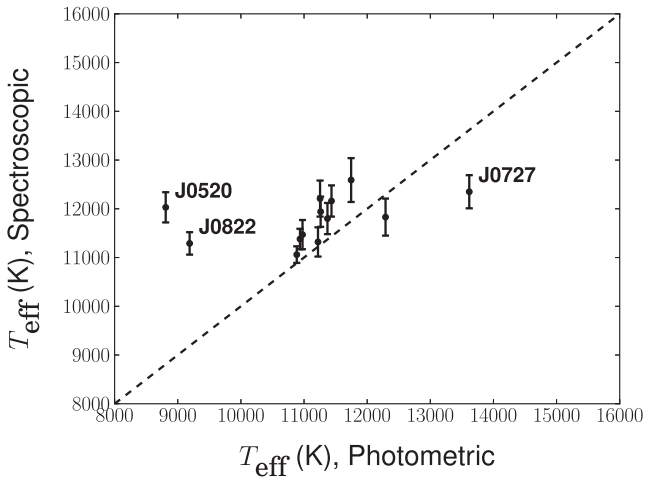

Figure 9. Comparison of the spectroscopic and photometric solutions for the effective temperature of all 13 targets in our sample. The diagonal dashed line shows one-to-one correspondence.

We detected a period of $P = 498.5 \pm 4.9$ s in J1015.[1] As only one night of data was available for J1015, follow-up observations are needed to verify this result. If the pulsation period is confirmed this result may contradict the suggestion made by Castanheira et al. (2013) that the DAV period distribution is bimodal and bereft of periods near ≈500 s. The addition of these high-mass DAVs nearly doubles the number of known ZZ Ceti WDs with $\log g > 8.5$ (Fig. 8), which is a significant population in terms of probing stellar evolution and exploring crystallization theory.

[1] Note Added in Proofs - Traditionally a WD is called a pulsator if variability is observed on two different nights. The variability seen in J1015 is consistent with pulsations in a DAV. However, follow-up photometry is required to confirm the pulsations in this object.

At $M = 1.16 \pm 0.03\,M_\odot$, J0840 is of similar mass to the previously discovered ultramassive DAVs, BPM 37093 ($M \approx 1.10\,M_\odot$) and GD 518 ($M = 1.20 \pm 0.03\,M_\odot$). We detect periods in J0840 ranging from roughly 180 to 800 s meanwhile pulsational periods of BPM 37093 lie in a narrow range of about 510–660 s (Kanaan et al. 2005) and those of GD 518 range from 425 to 595 s (Hermes et al. 2013). Our observed period range is consistent with the calculated period range for a $1.1\,M_\odot$ CO-core WD with $T_{\rm eff} = 12\,200$ K presented in fig. 9 of Montgomery & Winget (1999), which shows the periods of $l = 2$ modes for crystallized mass ratios ranging from 0 to 0.99.

Previous studies of BPM 37093, the most extensively observed high-mass DAV, have encountered difficulty with mode identification since its modes are both low amplitude and undergo amplitude modulation (Kanaan et al. 2005). Furthermore, amplitudes reported for GD 518 range from roughly 1 to 4 mma (Hermes et al. 2013). The dominant periods of pulsation for J0840 remained consistent within the errors between the four nights of available data over a period of about 3 months. We thus expect that J0840 undergoes stable pulsations of relatively high amplitude, which may facilitate mode identification. Hence, J0840 offers an excellent laboratory to probe core crystallization via asteroseismology. J0840 is likely the remnant of a star with a ZAMS mass of $\gtrapprox 7\,M_\odot$ and is thus expected to have a significantly crystallized ONe or ONeMg core.

Córsico et al. (2004) suggest that it should be possible to determine the core composition of DAVs based on their pulsation spectrum. They examine the adiabatic pulsational properties of $1.05\,M_\odot$ WD stars with CO and ONe cores and find that there are marked differences in the period spacing distributions depending on the core composition. The ONe-core models displayed significant non-uniformities in the forward period spacing and were also characterized by a larger mean period spacing than CO-models of the same temperature. The kinetic energy spectra of their ONe-core and CO-core models show significant differences as well.

With three or fewer periods of pulsation detected for these newly discovered DAVs we are unable to conduct an in-depth asteroseismological analysis on these objects. With future observations

and the identification of many more normal modes in the pulsation spectra of these DAVs, their total mass and hydrogen envelope mass can be measured. Further populating the high-mass end of the ZZ Ceti instability strip is paramount to the study of crystallization physics as the most massive DAVs are expected to have ∼90 per cent crystallized cores. J0840 is a most interesting DAV as it offers an unprecedented opportunity to constrain the evolution of intermediate-mass stars and the internal structure of a $1.16\,M_{\odot}$ WD.

ACKNOWLEDGEMENTS

We gratefully acknowledge the support of the NSF and NASA under grants AST-1312678, AST-1312983 and NNX14AF65G. This paper includes data taken at the McDonald Observatory of the University of Texas at Austin as well as the Apache Point Observatory 3.5-m telescope, which is owned and operated by the Astrophysical Research Consortium. This paper is partly based on observations obtained at the Gemini Observatory (acquired through the Gemini Science Archive and processed using the Gemini IRAF package), which is operated by the Association of Universities for Research in Astronomy, Inc., under a cooperative agreement with the NSF on behalf of the Gemini partnership: the National Science Foundation (USA), the National Research Council (Canada), CONICYT (Chile), Ministerio de Ciencia, Tecnología e Innovación Productiva (Argentina) and Ministério da Ciência, Tecnologia e Inovação (Brazil).

REFERENCES

Abazajian K. N. et al., 2009, ApJS, 182, 543
Abriksov A. A., 1960, Soviet Phys. JETP Lett., 12, 1254
Ahn C. P. et al., 2014, ApJS, 211, 17
Althaus L. G., García-Berro E., Isern J., Córsico A. H., 2005, A&A, 441, 689
Bergeron P., Ruiz M. T., Legget S. K., 1997, ApJS, 108, 339
Bevington P. R., 1969, Data Reduction and Error Analysis for the Physical Sciences. McGraw-Hill, New York
Bischoff-Kim A., Østensen R. H., Hermes J. J., Provencal J. L., 2014, ApJ, 794, 39
Brassard P., Fontaine G., 2005, ApJ, 622, 572
Breger M. et al., 1993, A&A, 271, 482
Castanheira B. G., Kepler S. O., 2009, MNRAS, 396, 1709
Castanheira B. G. et al., 2006, A&A, 450, 227
Castanheira B. G., Kepler S. O., Kleinman S. J., Nitta A., Fraga L., 2013, MNRAS, 430, 50
Córsico A. H., Althaus L. G., 2006, A&A, 454, 863
Córsico A. H., García-Berro E., Althaus L. G., Isern J., 2004, A&A, 427, 923
Dawson K. S. et al., 2013, AJ, 145, 10
Doherty C. L., Gil-Pons P., Siess L., Lattanzio J. C., Lau H. H. B., 2015, MNRAS, 446, 2599
Eisenstein D. J. et al., 2006, ApJS, 167, 40
Eisenstein D. J. et al., 2011, AJ, 142, 72
Fontaine G., Brassard P., 2008, PASP, 120, 1043
Fontaine G., Brassard P., Bergeron P., 2001, PASP, 113, 409
Giammichele N., Fontaine G., Brassard P., Charpinet S., 2016, ApJS, 223, 10
Gianninas A., Bergeron P., Fontaine G., 2005, ApJ, 631, 1100
Gianninas A., Bergeron P., Ruiz M. T., 2011, ApJ, 743, 138
Green E. M. et al., 2015, in Dufour P., Bergeron P., Fontaine G., eds, ASP Conf. Ser. Vol. 493, 19th European Workshop on White Dwarfs. Astron. Soc. Pac., San Francisco, p. 237
Gunn J. E. et al., 2006, AJ, 131, 2332
Hansen C. J., Van Horn H. M., 1979, ApJ, 233, 253
Harris H. C. et al., 2003, AJ, 126, 1023
Hermes J. J., Kepler S. O., Castanheira B. G., Gianninas A., Winget D. E., Montgomery M. H., Brown W. R., Harrold S. T., 2013, ApJ, 771, L2
Horowitz C. J., Schneider A. S., Berry D. K., 2010, Phys. Rev. Lett., 104, 231101
Kanaan A., Kepler S. O., Giovannini O., Diaz M., 1992, ApJ, 390, L89
Kanaan A., Kepler S. O., Winget D. E., 2002, A&A, 389, 896
Kanaan A. et al., 2005, A&A, 432, 219
Kepler S. O., Castanheira B. G., Saraiva M. F. O., Nitta A., Kleinman S. J., Mullally F., Winget D. E., Eisenstein D. J., 2005, A&A, 442, 629
Kepler S. O., Kleinman S. J., Nitta A., Koester D., Castanheira B. G., Giovannini O., Costa A. F. M., Althaus L., 2007, MNRAS, 375, 1315
Kepler S. O. et al., 2012, ApJ, 757, 177
Kepler S. O. et al., 2015, MNRAS, 446, 4078
Kepler S. O. et al., 2016, MNRAS, 455, 3413
Kilic M. et al., 2015, ApJ, 814, L31
Kirshnitz D. A., 1960, Soviet Phys. JETP Lett., 11, 365
Kleinman S. J. et al., 2004, ApJ, 607, 426
Kleinman S. J. et al., 2013, ApJS, 204, 5
Lamb D. Q., Van Horn H. M., 1975, ApJ, 200, 306
Lenz P., Breger M., 2005, Commun. Asteroseismol., 146, 53
Liebert J., Bergeron P., Holberg J. B., 2005, ApJS, 156, 47
Metcalfe T. S., Montgomery M. H., Kanaan A., 2004, ApJ, 605, L133
Montgomery M. H., O'donoghue D., 1999, Delta Scuti Star Newsletter, 13, 28
Montgomery M. H., Winget D. E., 1999, ApJ, 526, 976
Mukadam A. S. et al., 2004, ApJ, 607, 982
Mullally F., Thompson S. E., Castanheira B. G., Winget D. E., Kepler S. O., Eisenstein D. J., Kleinman S. J., Nitta A., 2005, ApJ, 625, 966
Renedo I., Althaus L. G., Miller Bertolami M. M., Romero A. D., Córsico A. H., Rohrmann R. D., García-Berro E., 2010, ApJ, 717, 183
Romero A. D., Córsico A. H., Althaus L. G., Kepler S. O., Castanheira B. G., Miller Bertolami M. M., 2012, MNRAS, 420, 1462
Romero A. D., Kepler S. O., Córsico A. H., Althaus L. G., Fraga L., 2013, ApJ, 779, 58
Salpeter E. E., 1961, ApJ, 134, 669
Segretain L., Chabrier G., Hernanz M., Garcia-Berro E., Isern J., Mochkovitch R., 1994, ApJ, 434, 641
Smee S. A. et al., 2013, AJ, 146, 32
Tremblay P.-E., Bergeron P., Gianninas A., 2011, ApJ, 730, 128
Tremblay P.-E., Ludwig H.-G., Steffen M., Freytag B., 2013, A&A, 559, A104
Van Horn H. M., 1968, ApJ, 151, 227
Winget D. E., Kepler S. O., 2008, ARA&A, 46, 157
Winget D. E., Kepler S. O., Kanaan A., Montgomery M. H., Giovannini O., 1997, ApJ, 487, L191
Winget D. E., Kepler S. O., Campos F., Montgomery M. H., Girardi L., Bergeron P., Williams K., 2009, ApJ, 693, L6
York D. G. et al., 2000, AJ, 120, 1579

This paper has been typeset from a TEX/LATEX file prepared by the author.